



Research Paper

CO₂ reforming of methane over supported LaNiO₃ perovskite-type oxides

R.C. Rabelo-Neto^a, H.B.E. Sales^b, C.V.M. Inocêncio^a, E. Varga^c, A. Oszko^c, A. Erdohelyi^c,
F.B. Noronha^a, L.V. Mattos^{b,*}

^a Instituto Nacional de Tecnologia, Av. Venezuela 82, 20081-312, Rio de Janeiro, Brazil

^b Universidade Federal Fluminense, Rua Passo da Pátria 156, 24210-240, Niterói, Brazil

^c Department of Physical Chemistry and Materials Science, University of Szeged, Aradi Vértanúk tere 1, H-6720 Szeged, Hungary

ARTICLE INFO

Keywords:

CO₂ reforming of methane
Biogas
LaNiO₃/CeSiO₂ catalyst
Hydrogen production

ABSTRACT

This work investigated the performance of supported LaNiO₃ perovskite-type oxides for the CO₂ reforming of methane. The methane and CO₂ conversion increased at the beginning of reaction for LaNiO₃ and LaNiO₃/Al₂O₃ catalysts. On the other hand, conversion remained quite constant for LaNiO₃/CeSiO₂. *in situ* XPS experiments under reaction conditions revealed that the metallic Ni particles were oxidized by CO₂ from the feed for LaNiO₃ and LaNiO₃/Al₂O₃ catalysts. Ceria support was preferentially oxidized, limiting the oxidation of the metallic phase. Raman spectroscopy and thermogravimetric analysis showed that carbon was formed mainly over LaNiO₃ and LaNiO₃/Al₂O₃ catalysts. Supporting LaNiO₃ over CeSiO₂ almost completely suppressed carbon deposition. *in situ* XPS experiments showed a continuous change of ceria oxidation states between Ce⁴⁺ and Ce³⁺ under reaction conditions. This result in a high oxygen mobility of ceria support that reacts with carbon, inhibiting the formation of nickel carbide and consequently the nucleation and growth of carbon filaments.

1. Introduction

Biogas is produced by anaerobic digestion or fermentation of organic matter such as sewage sludge, municipal sewage water, etc. Biogas is a complex gaseous mixture containing mainly CH₄ and CO₂. Therefore, the emission of biogas to the atmosphere may contribute significantly to the greenhouse gas effect. However, only a small portion of this biogas is used. In these cases, this gaseous mixture is used for heat or electricity generation through combustion process. The production of hydrogen from biogas for energy generation through fuel cells is a promising technology. In this approach, the biogas is converted to synthesis gas by the CO₂ reforming of methane process (dry reforming of methane – DRM) followed by H₂ purification steps.

The DRM has been intensively investigated for the production of synthesis gas [1–5]. One of the main barriers of the dry reforming technology is the catalyst deactivation that occurs due to carbon deposition during the high temperature process [6–8]. Therefore, the development of a catalyst resistant to carbon deposition during CO₂ reforming of CH₄ is one of the main issues of this technology.

The carbon deposition in this reaction strongly depends on the type of metal. Ni-based catalysts have been extensively studied for the DRM due to its low cost and high activity but this metal is prone to coking [9–11]. The nickel particle size significantly influences the nucleation rate of carbon. The initiation step for carbon formation is more difficult

for smaller particle sizes [12]. A critical ensemble size (ensembles of 6–7 atoms) was proposed, below which carbon formation does not occur. Therefore, one approach to minimize or inhibit carbon formation is to control metal particle size by the appropriated selection of catalyst preparation method.

Mixed oxides such as perovskite-type oxides (with general formula ABO₃) have been reported as promising precursors for DRM catalysts. Dispersed metallic particles are obtained, when this mixed oxide were reduced [13,14]. There are many papers in the literature reporting the use of perovskite-type oxide precursor as catalysts for DRM [13–16]. However, the high reduction temperatures required for the removal of metal from the perovskite structure limits the strategy to obtain highly dispersed metallic particles. This may be overcome by the deposition of perovskite-type oxides over an oxide with high surface area. However, there are only few studies about the use of supported perovskite-type oxides for DRM [17,18].

The support plays a key role on the mechanism of DRM. Supports like ceria participate in the dissociative adsorption of CO₂ near the metal particles, transferring oxygen to the surface of the metallic particle containing carbon deposits [19–22]. Thereby, the support promotes the mechanism of carbon removal from the metal, inhibiting catalyst deactivation. The addition of dopants to ceria increases the oxygen mobility of the support [23]. Zirconia is the mostly studied ceria dopant due to its use on the automotive emission control catalysts

* Corresponding author.

E-mail addresses: lisianemattos@yahoo.com.br, lisiane@vm.uff.br (L.V. Mattos).

<http://dx.doi.org/10.1016/j.apcatb.2017.09.022>

Received 23 June 2017; Received in revised form 8 September 2017; Accepted 10 September 2017

Available online 11 September 2017

0926-3373/ © 2017 Elsevier B.V. All rights reserved.

whereas silica is less used. The addition of silica significantly decreases the crystallite size of ceria, increasing its oxygen mobility [24]. Then, the deposition of perovskite-type oxide over a high surface area ceria-mixed oxide could inhibit carbon deposition by promoting Ni dispersion as well as providing oxygen to the metallic surface, which prevents carbon accumulation.

Therefore, the aim of this work is to study the performance of supported Ni-based catalysts prepared from perovskite-type oxide precursor for the production of hydrogen through DRM. *in situ* X-ray diffraction (XRD), and *in situ* X-ray photoelectron spectroscopy (XPS) were performed to monitor the changes in the structure and surface of the catalysts during reduction and reaction. In order to evaluate the formation of carbonaceous deposits on the catalyst surface during the reaction, thermogravimetric (TG) analysis and Raman spectroscopy analyses were carried out.

2. Experimental

2.1. Catalysts preparation

The LaNiO_3 perovskites were prepared, using a combustion method. Urea and nitrates of nickel and lanthanum were used as a fuel and oxidizers, respectively [25]. The ratio of the total valences of fuel to the total valence of oxidizers (ϕ) was 0.7. Then, an aqueous suspension containing the adequate quantity of urea and nitrate precursors was stirred on a heating plate until spontaneous ignition. The samples obtained were calcined in a muffle at 1073 K during 1 h.

Alumina (Puralox-Sasol) support was calcined at 1073 K for 6 h. For the preparation of CeO_2 - SiO_2 support (CeSiO_2), initially, SiO_2 (Aerosil 200 – Degussa) was dissolved in an alkaline solution containing potassium hydroxide. Then, the solution obtained was added to a solution of ammonium hydroxide. Therefore, the precipitation was carried out by adding a solution of $(\text{NH}_4)_2\text{Ce}(\text{NO}_3)_6 \cdot 6\text{H}_2\text{O}$ (Aldrich 98%). After that, the precipitate was maintained under stirring for 30 min, washed until pH = 7 and dried at 383 K for 12 h. The samples were calcined at 1073 K for 5 h under air flow. The Ce/Si molar ratio obtained was 3.0.

For the supported LaNiO_3 samples, a suspension containing an ethanol solution, LaNiO_3 perovskite and supports (Al_2O_3 or CeSiO_2) was prepared. At first, the ethanol solution was maintained in an ultrasonic bath for 20 min. Then, the perovskite and Al_2O_3 or CeSiO_2 supports were added to the ethanol solution that was kept under stirring for 30 min. Thereafter, the ethanol was taken out using a rotary evaporator. After removal of ethanol, the sample was submitted to drying at 383 K and calcination at 1073 K (10 K/min) for 5 h. The supported LaNiO_3 samples contained 30 wt.% of perovskite. Then, three different materials were obtained: LaNiO_3 , $\text{LaNiO}_3/\text{Al}_2\text{O}_3$ and $\text{LaNiO}_3/\text{CeSiO}_2$.

2.2. X-ray fluorescence (XRF)

In order to determine the chemical composition of each sample, the analysis of XRF were performed, using a Bruker Wavelength Dispersive X-Ray Fluorescence Spectrometer (WD-XRF) S8 Tiger with a rhodium tube operated at 4 kW. It was used 300 mg of samples in power form and a semi-quantitative method (QUANT-EXPRES/Bruker).

2.3. BET surface area

A Micromeritics ASAP 2020 analyzer was used for the measurements of the BET surface areas of the samples. For this, the nitrogen adsorption was carried out at the boiling temperature of liquid nitrogen.

2.4. *In situ* X-ray diffraction (XRD)

In situ XRD analyses of samples were performed in a furnace installed into a Huber goniometer operating in Bragg–Brentano geometry

(θ – 2θ) at the XPD–10 B beamline of the Brazilian Synchrotron Light Laboratory (LNLS). The diffractograms were obtained by a Mythen – 1 K detector (Dectris) in a 2θ range of 24° to 54° , using a wavelength of 1.5507 Å. The analyses were carried out, during the reduction treatment and DRM reaction. For reduction treatment, the samples were heated from 298 to 1023 K (10 K/min) under a 5% H_2/He mixture and maintained at 1023 K for 1 h. After that, the samples were heated under helium to 1073 K and remained at this temperature for 30 min. In the case of DRM reaction, the samples were submitted to a mixture containing 20% CH_4 , 20% CO_2 and 60% He at 1073 K for 1 h. The Scherrer equation was used to calculate the average crystallite size of metallic Ni during reduction under H_2 at different temperatures and under reaction conditions treatment.

2.5. X-ray photoelectron spectroscopy (XPS)

The XPS experiments were carried out in a SPECS instrument equipped with a PHOIBOS 150 MCD 9 analyzer operated in the FAT mode at a pass energy of 20 eV. Non-monochromated Al K α radiation (1486.6 eV) was used to provoke electron emission from the samples and the X-ray source worked at 210 W and 14 kV. Three or five scans were summed to get a single spectrum. The pressure during the measurements was kept in the 10^{-9} mbar range. The binding energies were referenced to Ni 3p (66.6 eV) for LaNiO_3 , Al 2p (74.5 eV) for $\text{LaNiO}_3/\text{Al}_2\text{O}_3$ and to the u'' (Burroughs notation) component of the Ce 3d spectrum (916.6 eV) for $\text{LaNiO}_3/\text{SiCeO}_2$.

For deconvolution, curved type background was set provided by the CasaXPS software package. Because of the complexity of the La 3d region, the peak envelope of the La $3d_{5/2}$ component was fitted to the La $3d_{3/2}$ constituent.

The samples were previously reduced under pure hydrogen (30 mL/min) at 1023 K for 1 h, purged under N_2 at the same temperature for 30 min and cooled to 298 K. Then, the reactor was maintained at 203 K for 1 h, using a mixture of isopropyl alcohol and liquid nitrogen and the catalyst was passivated with a 5% O_2/He mixture.

Reactions at atmospheric pressure in flowing gas were carried out for the XPS studies in a high-pressure (catalysis) cell that was attached to the analyzing chamber of the instrument with a gate valve. The pre-reduced samples underwent an additional reduction in H_2 at 773 K with 45 mL/min flow rate (post-reduction). The reactions with $\text{CH}_4 + \text{CO}_2$ (1:1) gas mixture were performed at 550 °C with a flow rate of 100 mL/min. The treatment was interrupted after the 5th, 30th and 120th minute of the reaction to take XP spectra. The samples were heated up to the reaction temperature and cooled back to room temperature in flowing N_2 . After reaching room temperature the catalysis cell was evacuated and the samples were moved back to the analysis chamber of the XPS instrument.

2.6. Reaction conditions

CO_2 reforming of methane was performed in a fix-bed reactor at atmospheric pressure. In order to avoid hot spot formation or temperature gradients, samples were diluted with quartz (quartz/catalyst ratio of 4.0). Prior to reaction, the sample was reduced under H_2 at 1023 K for 1 h and then heated to the reaction temperature under N_2 . A reactant mixture containing methane and carbon dioxide with a $\text{CH}_4:\text{CO}_2$ molar ratio of 1 and a total flow rate of 100 mL/min was used. The exit gases were analyzed using a gas chromatograph (Agilent 6890) equipped with a thermal conductivity detector and a Carboxen 1010 column (Supelco). The CH_4 and CO_2 conversion and product distribution were calculated from:

$$X_i = \frac{(n_i)_{\text{feed}} - (n_i)_{\text{exit}}}{(n_i)_{\text{feed}}} \times 100 \quad (1)$$

$$S_x = \frac{(n_x)_{\text{produced}}}{(n_{\text{total}})_{\text{produced}}} \times 100 \quad (2)$$

where $i = \text{CH}_4$ or CO_2 and $(n_x)_{\text{produced}} = \text{mols of } x \text{ produced}$ ($x = \text{hydrogen, CO or H}_2\text{O}$) and $(n_{\text{total}})_{\text{produced}} = \text{mols of H}_2 + \text{mols of CO} + \text{mols of H}_2\text{O}$.

Two different experiments were carried out. In the first one, the amount of catalyst was varied to obtain low methane conversions (around 10–20%) in order to determine the turnover frequency (TOF) at 823 K. In the second series of experiments, long-term tests were performed at 1073 K in order to investigate the stability of the catalysts. In this case, different amounts of catalysts were used to have the same Ni weight in all runs.

Forward CH_4 turnover rates (r_f) (Eq. (3)) were obtained from measured rates (r_n) under differential conditions, considering the approach to equilibrium in CO_2 (Eq. (4)) reforming reaction as proposed by Wei and Iglesia [26]:

$$r_n = r_f (1 - \eta) \quad (3)$$

$$\eta = \frac{[P_{\text{CO}}]^2 [P_{\text{H}_2}]^2}{[P_{\text{CH}_4}] [P_{\text{CO}_2}]} \cdot \frac{1}{K_{\text{eq}}} \quad (4)$$

Where K_{eq} is the equilibrium constant for dry reforming of methane that is given by the van't Hoff equation [27].

Turnover frequencies (TOF) for the DRM (Eq. (5)) were calculated taking into account the Ni dispersion (estimated using $D = 1/d$ [28], where d was calculated from Scherrer equation as previously described).

$$\text{TOF} = r_f / \text{Ni surface atoms} \quad (5)$$

2.7. Thermogravimetric analysis (TG)

The determination of quantity of carbon formed during DRM was made by Thermogravimetric analysis of the used catalysts. The experiments were performed in a TA Instruments equipment (SDT Q600). The weight change observed for spent catalyst (10 mg) during heating under air from room temperature to 1273 K (20 K/min) was measured.

2.8. Raman spectroscopy

Raman spectroscopy was used to characterize the nature of carbon formed after reaction. The spectra were recorded at room temperature using a Horiba LabRam HR-UV800/Jobin-Yvon spectrometer, equipped with He-Ne laser ($\lambda = 632 \text{ nm}$) of 10 mW power, a CCD detector and an Olympus BX41 microscope with objective lens of 100 \times .

3. Results and discussion

3.1. Catalyst characterization

Table 1 lists the Ni, La_2O_3 , Al_2O_3 and CeO_2 content of all samples. The Ni loading obtained by XRF analysis was close to the nominal value for all samples studied (Bulk: 23.0; supported samples: 6.9 wt.% Ni). The BET surface area of Al_2O_3 and CeSiO_2 were 150 and 51 m^2/g ,

Table 1
BET surface area and chemical composition of the catalysts.

Sample	Surface area (m^2/g)	Chemical composition (%)				
		Ni	La	Al	Ce	Si
LaNiO_3	4	23.7	56.4	–	–	–
$\text{LaNiO}_3/\text{Al}_2\text{O}_3$	102 (150) ^a	6.9	16.4	37.6	–	–
$\text{LaNiO}_3/\text{CeSiO}_2$	37 (51) ^a	7.3	17.3	–	51.6	3.2

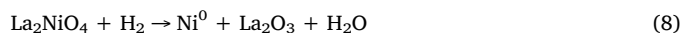
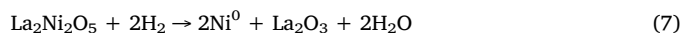
^a The values in the parentheses correspond to surface area of support.

respectively. The surface area of silica-doped ceria is high in comparison to the values reported in the literature for undoped CeO_2 samples calcined at high temperature (1073 K) ($< 10 \text{ m}^2/\text{g}$) [29]. Rocchini et al. [30] also observed that doping ceria with different silica contents increased the surface area of ceria. According to Hu et al. [31], doping ceria with Si improves the resistance to sintering of ceria because the Si interacts with the surface of CeO_2 nanocrystallites by forming $\text{Ce}-\text{O}-\text{Si}$ units, thus hindering $\text{Ce}-\text{O}-\text{Ce}$ forming condensation reactions.

Unsupported LaNiO_3 exhibited a very low surface area ($< 10.0 \text{ m}^2/\text{g}$) that could be attributed to the high calcination temperature used [25]. The deposition of LaNiO_3 over Al_2O_3 and CeSiO_2 supports reduced the surface area of the supports.

Figs. 1 a, 2 a and 3 a show the in situ X-ray diffraction patterns obtained during reduction and DRM reaction for LaNiO_3 , $\text{LaNiO}_3/\text{Al}_2\text{O}_3$ and $\text{LaNiO}_3/\text{CeSiO}_2$ samples. The diffractograms recorded at specific temperatures are displayed in Figs. 1 b, 2 b and 3 b. The XRD patterns of the calcined LaNiO_3 and $\text{LaNiO}_3/\text{Al}_2\text{O}_3$ samples showed the diffraction lines corresponding to the LaNiO_3 rhombohedral phase (PDF 33-0711). In addition, the lines typical of NiO (PDF 44-1159) and La_2NiO_4 (PDF 34-0314) phases were also observed. Silva et al. [25] also reported the presence of the lines typical of the La_2NiO_4 phase in the diffractogram of a LaNiO_3 perovskite-type oxide prepared by the combustion method. La_2NiO_4 can be described as a succession of perovskite layers alternating with LaO layers [32]. For the $\text{LaNiO}_3/\text{CeSiO}_2$ sample, there were the lines corresponding to both CeO_2 with cubic structure (PDF 34-0394) and LaNiO_3 rhombohedral phase. It was not possible to distinguish the LaNiO_3 perovskite phase due to the overlapping of its lines by the ones typical of CeO_2 . However, the presence of the LaNiO_3 perovskite phase can be confirmed comparing the relative intensity of diffraction lines at 2θ around 28.6 and 33.0° with that reported in the literature for CeO_2 cubic phase. The diffractogram of $\text{LaNiO}_3/\text{CeSiO}_2$ sample did not provide any evidence for the presence of crystalline SiO_2 . Rocchini et al. [30] reported that the diffractograms of calcined silica-doped ceria samples with different silica loading revealed the presence of crystalline ceria and amorphous silica.

Fig. 1 shows the in situ X-ray diffraction patterns obtained during reduction for LaNiO_3 . Increasing the temperature to 473 K did not produce any significant change in the diffractograms. However, the lines characteristic of LaNiO_3 phase were shifted to lower 2θ positions when the temperature was increased to 573 K. This result has been reported in the literature and it is attributed to the reduction of Ni^{3+} in the perovskite structure to Ni^{2+} (eq. (6)) with the formation of a $\text{La}_2\text{Ni}_2\text{O}_5$ phase (PDF 36-1230) [25]. Further increase to 678 K resulted in the disappearance of the line corresponding to NiO , whereas a new line is observed at $2\theta = 44.3^\circ$, indicating that NiO was completely reduced to metallic Ni. At 783 K, the intensity of the lines attributed to $\text{La}_2\text{Ni}_2\text{O}_5$ phase strongly decreased whereas the intensity of the line corresponding to Ni^0 phase increased. Furthermore, the lines characteristic of La_2O_3 phase (PDF 33-0710) are clearly observed, indicating that $\text{La}_2\text{Ni}_2\text{O}_5$ phase was destroyed, producing metallic Ni and lanthanum oxide (eq. (7)). After heating the sample at 887 K, the diffraction lines of the perovskite phases were no longer detected and the intensities of the lines of Ni^0 and La_2O_3 phases increased. This result suggests that the $\text{La}_2\text{Ni}_2\text{O}_5$ and La_2NiO_4 phases were completely destroyed at this temperature (Eqs. (7) and (8)). Increasing the reduction temperature to 1023 K only increased the intensities of the lines of Ni^0 and La_2O_3 phases, indicating metallic Ni particles sintered.



The changes observed in the diffractograms during reduction of $\text{LaNiO}_3/\text{Al}_2\text{O}_3$ sample (Fig. 2b) were quite similar to those of LaNiO_3

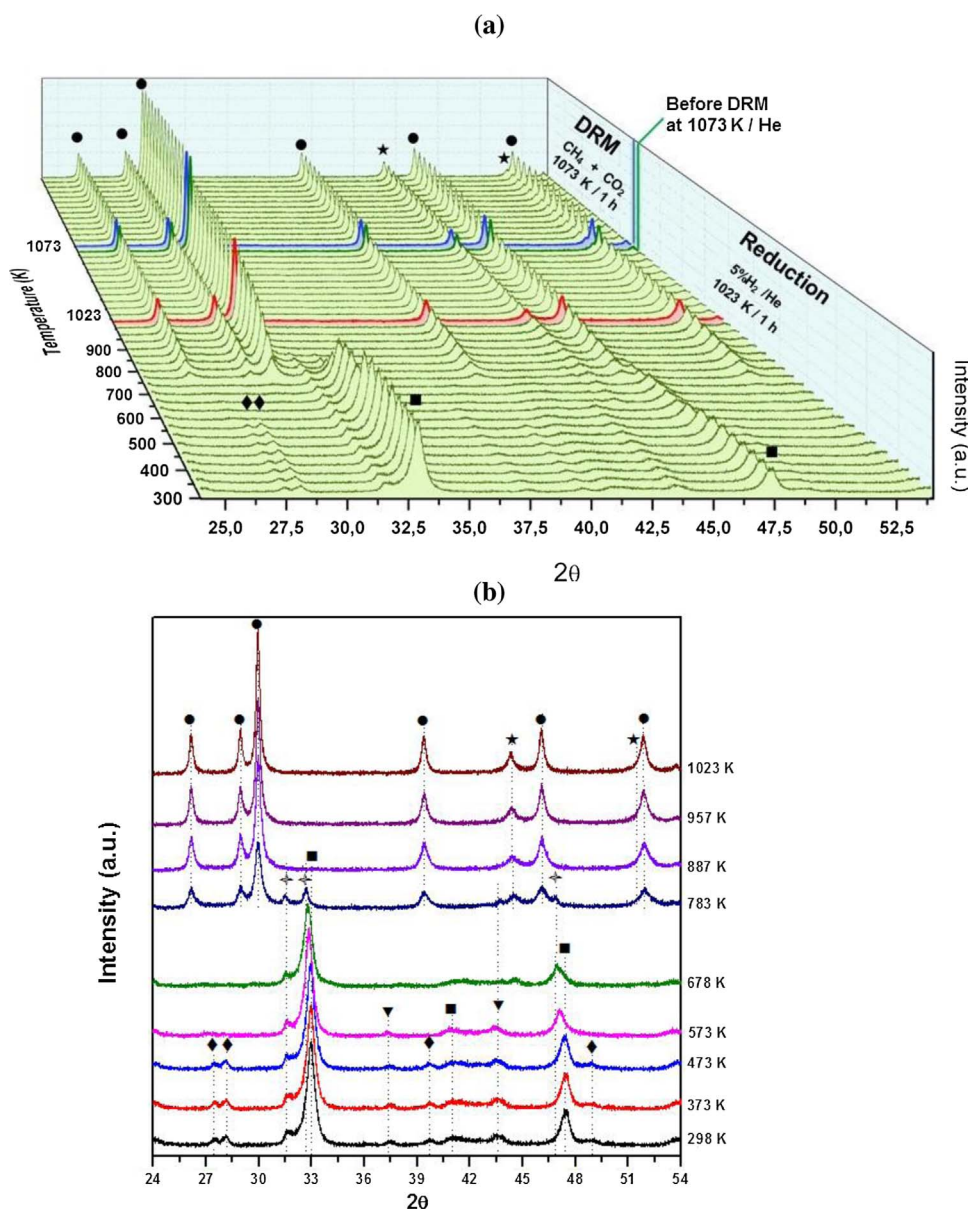


Fig. 1. X-ray diffraction patterns obtained for LaNiO_3 (a) during reduction from room temperature to 1023 K; (b) selected temperatures. (◆) $\text{La}(\text{OH})_3$; (■) La_2NiO_4 ; (●) NiO ; (●) La_2O_3 ; (★) Ni^0 .

(Fig. 1b). The formation of $\text{La}_2\text{Ni}_2\text{O}_5$ phase occurred at 573 K, as evidenced by the shift of the lines characteristic of LaNiO_3 phase to lower 2θ positions. At 783 K, LaNiO_3 and $\text{La}_2\text{Ni}_2\text{O}_5$ phases were completely destroyed and only the lines corresponding to La_2O_3 and La_2NiO_4 were detected. This perovskite phase was no longer observed at 887 K. The lines attributed to NiO disappeared at 678 K, whereas a shoulder appeared at around $2\theta = 44.5^\circ$ that is related to the formation of metallic Ni. Increasing the reduction temperature to 1023 K led to an increase in the intensities of the lines of La_2O_3 and Ni^0 .

For $\text{LaNiO}_3/\text{CeSiO}_2$ sample (Fig. 3b), the increase in the reduction temperature from 298 to 678 K produced a shift to lower 2θ positions on the lines corresponding to LaNiO_3 and CeO_2 phases. This result could be attributed to the formation of $\text{La}_2\text{Ni}_2\text{O}_5$ as well as the reduction of CeO_2 to CeO_x . Taking into account that the line characteristic of CeO_2 (111) ($2\theta = 28.60^\circ$) did not modify, this shift is likely due to the formation of $\text{La}_2\text{Ni}_2\text{O}_5$ phase. The La_2NiO_4 phase was completely destroyed at 887 K. The lines typical of metallic Ni were observed at 678 K and the increase in the temperature increased their intensities. At 1023 K, the diffractogram exhibits the lines of La_2O_3 , La_2NiO_4 and Ni^0 .

Table 2 lists the average crystallite size of Ni^0 obtained during reduction of the samples at different temperatures. After reduction at

811–838 K, LaNiO_3 sample showed a Ni crystallite size of 10 nm. The increase in the reduction temperature to 1023 K strongly increased the Ni crystallite size, indicating that the reduction treatment significantly sintered the metal particles. For $\text{LaNiO}_3/\text{Al}_2\text{O}_3$ sample, it was also observed a growth of Ni particles when the catalyst was heated under hydrogen to 1023 K but this effect was less significant than that of unsupported catalyst. However, only a slight increase in the average crystallite size of Ni^0 occurred for the $\text{LaNiO}_3/\text{CeSiO}_2$ sample. This result revealed that the interaction between metallic Ni and ceria inhibited metal sintering.

Consequently, in situ XRD experiments showed that the LaNiO_3 perovskite-type oxide phase was destroyed during reduction and the working catalyst is nickel dispersed over lanthanum. However, the nomenclature “ LaNiO_3 catalyst” is retained during the discussion of the catalytic results to emphasize that the LaNiO_3 perovskite-type oxide phase was the precursor to the catalyst.

3.2. CO_2 reforming of methane

Turnover frequencies of methane conversion were determined from experiments in which methane conversion was maintained between 10

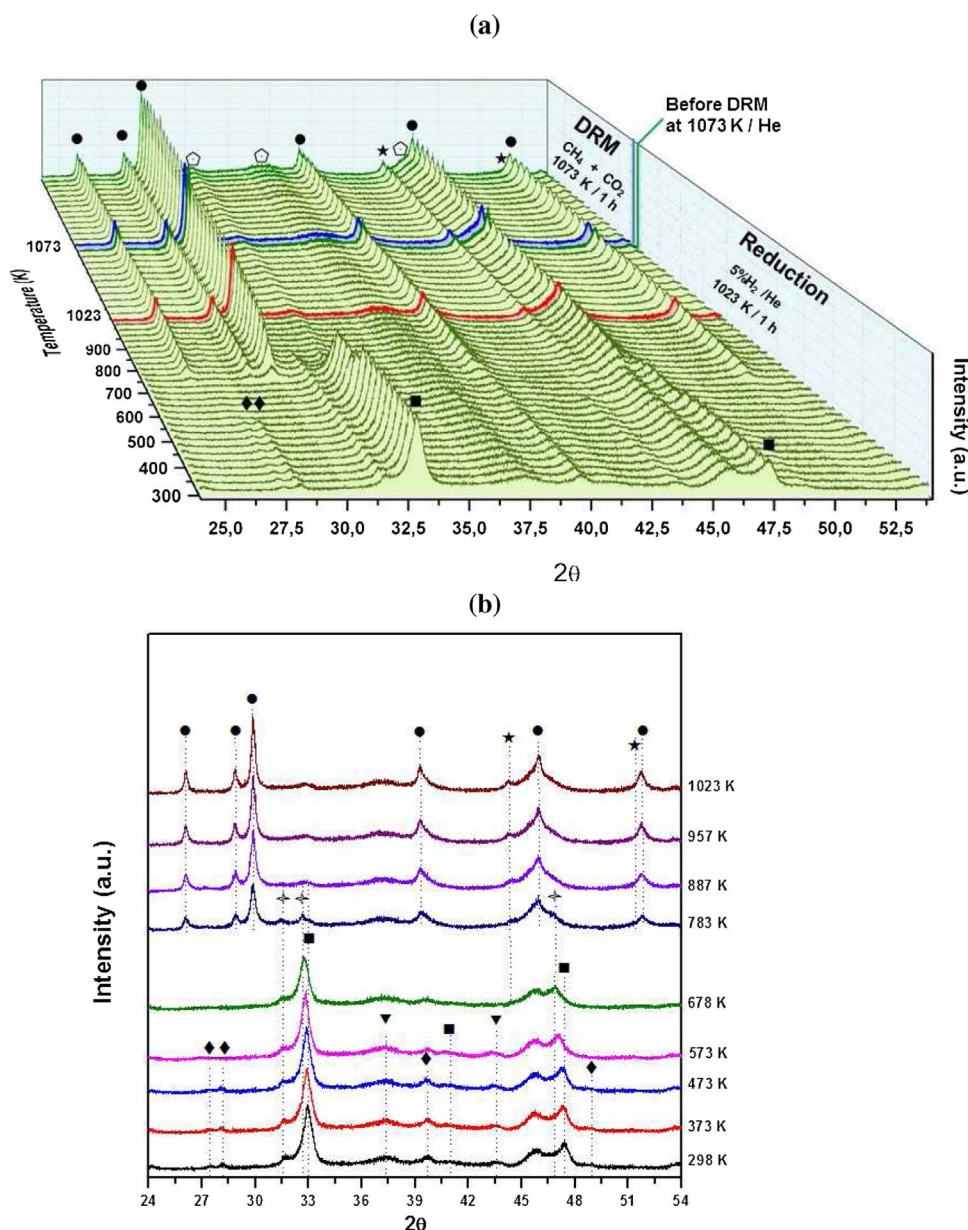


Fig. 2. X-ray diffraction patterns obtained for $LaNiO_3/Al_2O_3$ (a) during reduction from room temperature to 1023 K; (b) selected temperatures. (■) $LaNiO_3$; (◆) La_2NiO_4 ; (●) NiO ; (●) La_2O_3 ; (★) Ni^0 ; (○) Al_2O_3 .

and 20%, taking into account the dispersion of the catalysts measured by in situ XRD. The values of the initial rate and TOF at 823 K are listed in Table 3. The TOF of all catalysts remained constant at around $0.63\text{--}1.55\text{ s}^{-1}$ that is expected since they have approximately the same dispersion (2–4%). These results agree very well with the work of Wei and Iglesia [26], who obtained TOF for DRM at 823 K around 2.0 s^{-1} over Ni/MgO catalyst.

In order to investigate the long-term stability of the catalysts for DRM, the reaction was carried out at 1073 K for 24 h under $CH_4/CO_2 = 1.0$. The methane and CO_2 conversions as a function of time on stream (TOS) obtained for the CO_2 reforming of CH_4 at 1073 K over $LaNiO_3$ and supported $LaNiO_3$ catalysts are shown in Fig. 4. $LaNiO_3$ catalyst exhibited the lowest initial methane and CO_2 conversion (25 and 35%, respectively) that increased continuously during reaction. After 10 h TOS, the run was interrupted due to the strong increase of pressure drop in the catalyst bed. For $LaNiO_3/Al_2O_3$ catalyst, methane and CO_2 conversion increased and leveled off after 4 h of TOS. The performance of $LaNiO_3/CeSiO_2$ catalyst was quite different. In this case, the methane and CO_2 conversion only slightly increased during the first 6 h TOS and then remained constant at around 58% (CH_4) and 70%

(CO_2) during 24 h of TOS. Regarding selectivity to products, hydrogen and CO were the main products obtained with small amounts of water. For $LaNiO_3$ catalyst, the H_2/CO ratio continuously increased from 0.24 to 0.72 (Fig. 5). In the case of $LaNiO_3/Al_2O_3$ catalyst, the H_2/CO ratio was 0.48 at the beginning of reaction and increased during reaction, levelling off at 0.67. For $LaNiO_3/CeSiO_2$ catalyst, H_2/CO ratio slightly increased and it was around 0.60 after 24 h of TOS. For all catalysts, the H_2/CO ratio followed the same trend observed for methane and CO_2 conversion. The higher conversion of CO_2 than the conversion of methane, the values of H_2/CO ratio less than 1.0 and the formation of water are likely due to the reverse of the water-gas shift reaction. Faria et al. [33] reported the same results for DRM over of $Ni/Ce_xZr_{1-x}O_2/Al_2O_3$.

The DRM reaction was also performed at 1073 K and a $CH_4/CO_2 = 1.3$. The range used for CH_4/CO_2 molar ratio (1.0–1.3) in our work is the typical variation of a biogas produced in a landfill. Fig. 6 shows the methane and CO_2 conversions as a function of TOS obtained for the CO_2 reforming of CH_4 at 1073 K and $CH_4/CO_2 = 1.3$ over supported $LaNiO_3$ catalysts. In this case, the run was ended after 3 h of TOS due to the strong increase in the pressure drop in the catalyst bed

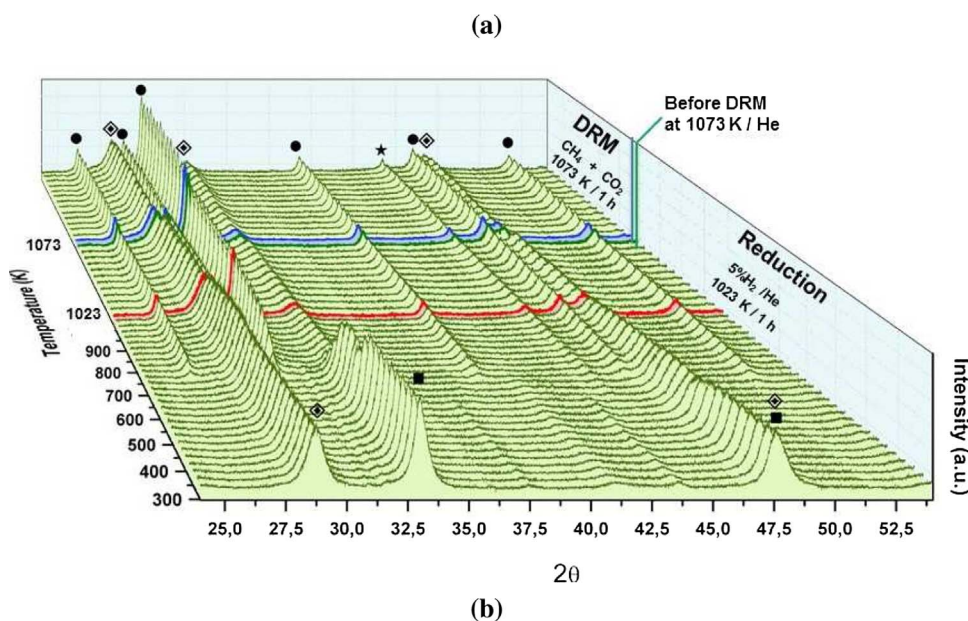


Fig. 3. X-ray diffraction patterns obtained for LaNiO₃/CeSiO₂ (a) during reduction from room temperature to 1023 K; (b) selected temperatures. (■) LaNiO₃; (◆) La₂NiO₄; (●) NiO; (★) La₂O₃; (★) Ni⁰; (⬇) CeO₂.

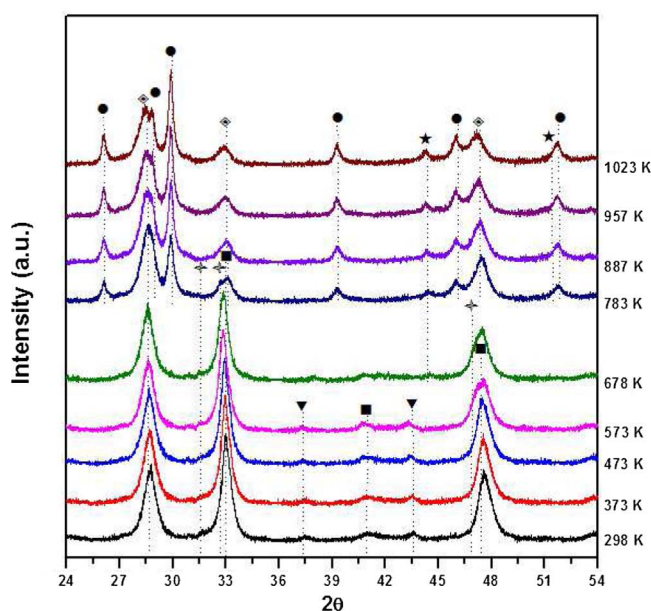


Table 2

Crystallite size of Ni⁰ calculated through X-ray diffraction patterns obtained during reduction under H₂ at different temperatures and under reaction conditions.

Catalysts	d _{Ni} (nm)					
	Reduction 811–838 K	Reduction 887–892 K	Reduction 973–992 K	Reduction 1023 K	Under He 1073 K	Reaction 1073 K/1h
LaNiO ₃	10.0	11.9	19.5	26.3	46.2	48.4
LaNiO ₃ /Al ₂ O ₃	15.4	18.3	21.9	25.7	40.5	44.1
LaNiO ₃ /CeSiO ₂	15.4	15.6	17.9	19.8	27.7	30.3

for LaNiO₃/Al₂O₃ catalyst. The methane and CO₂ conversions only slightly increased during the reaction for LaNiO₃/CeSiO₂ catalyst, as it was previously observed for the run under the CH₄/CO₂ = 1.0. In comparison with the experiment using a CH₄/CO₂ = 1.0, the increase in the CH₄/CO₂ molar ratio increased the methane and CO₂ conversions and the H₂/CO ratio and decreased the formation of water, indicating that the occurrence of RWGS reaction is less important.

The variation of methane and CO₂ conversions during the DRM has been reported in the literature for Ni-based catalysts [33,34]. Takanabe et al. [34] also observed the increase of methane conversion during

DRM over Ni and Co supported on TiO₂ catalysts. They proposed that metallic Ni particles were oxidized by the CO₂ of the feed at the beginning of the reaction. Then, the syngas produced during the dry reforming reaction reduced the NiO particles formed to metallic Ni particles, increasing methane conversion. Faria et al. [33] studied the performance of Ni/Ce_xZr_{1-x}O₂/Al₂O₃ (x = 0.5; 0.75; 1.0) catalysts for the production of synthesis gas through CO₂ reforming of CH₄. Ni/Al₂O₃ and Ni/CeO₂/Al₂O₃ catalysts showed an increase of methane and CO₂ conversion at the beginning of reaction. For Ni/Ce_{0.75}Zr_{0.25}O₂/Al₂O₃ and Ni/Ce_{0.50}Zr_{0.50}O₂/Al₂O₃ catalysts, the conversion remained

Table 3
Crystallite size of Ni⁰ (d_{Ni}), metallic dispersion (D), initial reaction rate and TOF of DRM.

Catalyst	d_{Ni} (nm) ^a	D (%) ^b	Initial rate (mol/min/g _{Ni})	TOF (s ⁻¹)
LaNiO ₃	46	2	0.018	0.87
LaNiO ₃ /Al ₂ O ₃	41	2	0.032	1.55
LaNiO ₃ /CeSiO ₂	28	4	0.026	0.63

^a Calculated using the Scherrer equation and the most intense line typical of Ni⁰ (111) at $2\theta = 44.5^\circ$ after heating under He to 1073 K.

^b Estimated from Ni crystallite size using $D = 1/d_{Ni}$ [28].

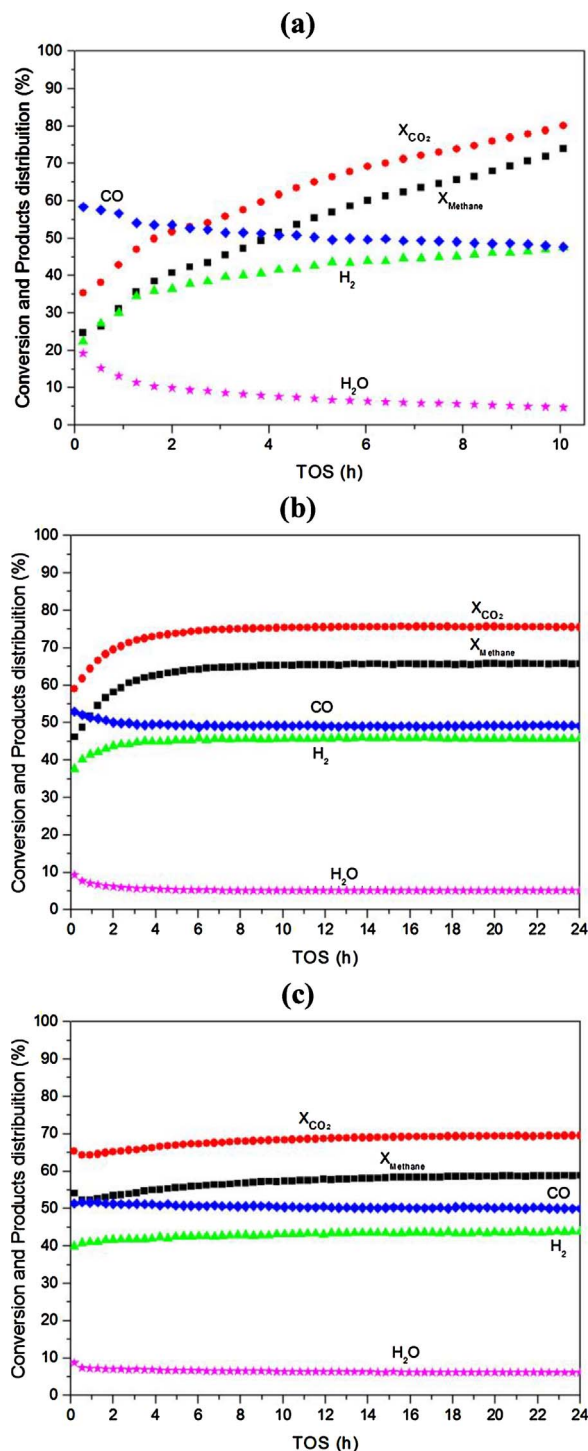


Fig. 4. Methane and CO₂ conversion versus TOS for CO₂ reforming of methane at 1073 K and CH₄/CO₂ = 1.0 over (a) LaNiO₃; (b) LaNiO₃/Al₂O₃; (c) LaNiO₃/CeSiO₂.

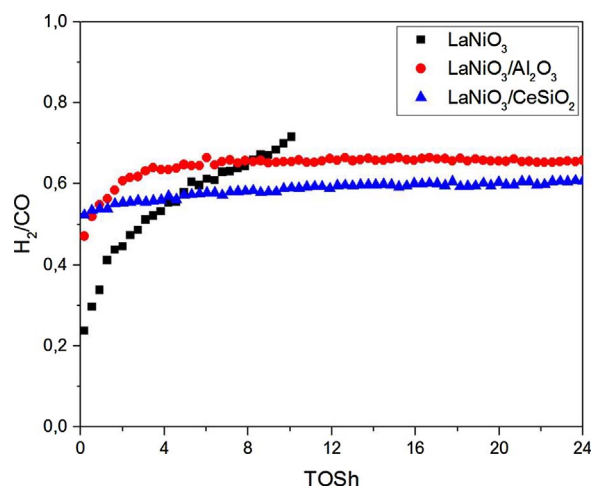


Fig. 5. H₂/CO molar ratio as a function of TOS for CO₂ reforming of methane at 1073 K and CH₄/CO₂ = 1.0 over (a) LaNiO₃; (b) LaNiO₃/Al₂O₃; (c) LaNiO₃/CeSiO₂.

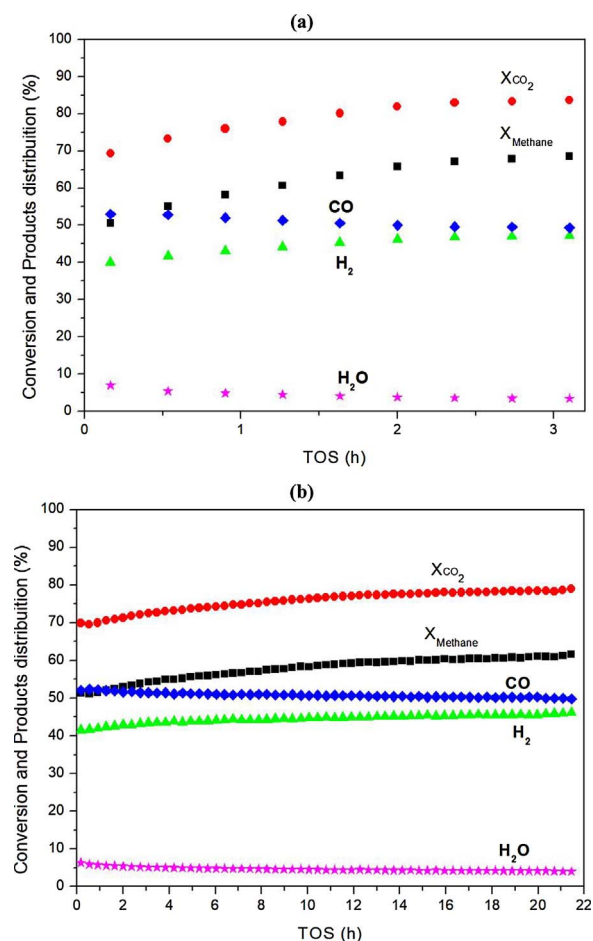


Fig. 6. Methane and CO₂ conversion versus TOS for CO₂ reforming of methane at 1073 K and CH₄/CO₂ = 1.3 over (a) LaNiO₃/Al₂O₃; (c) LaNiO₃/CeSiO₂.

quite constant during the reaction. They carried out an XRD experiment after exposing the Ni/Al₂O₃ catalyst to CO₂ stream in order to investigate the evolution of the phases present in the catalyst. After the exposition of the catalyst to CO₂, the line characteristic of Ni⁰⁰ was no longer observed and the appearance of the line related to NiO phase was noticed. This result was associated with the oxidation of metallic Ni particles by CO₂ from the feed. For Ni/Ce_{0.75}Zr_{0.25}O₂/Al₂O₃ and Ni/Ce_{0.50}Zr_{0.50}O₂/Al₂O₃ catalysts, ceria-zirconia support was

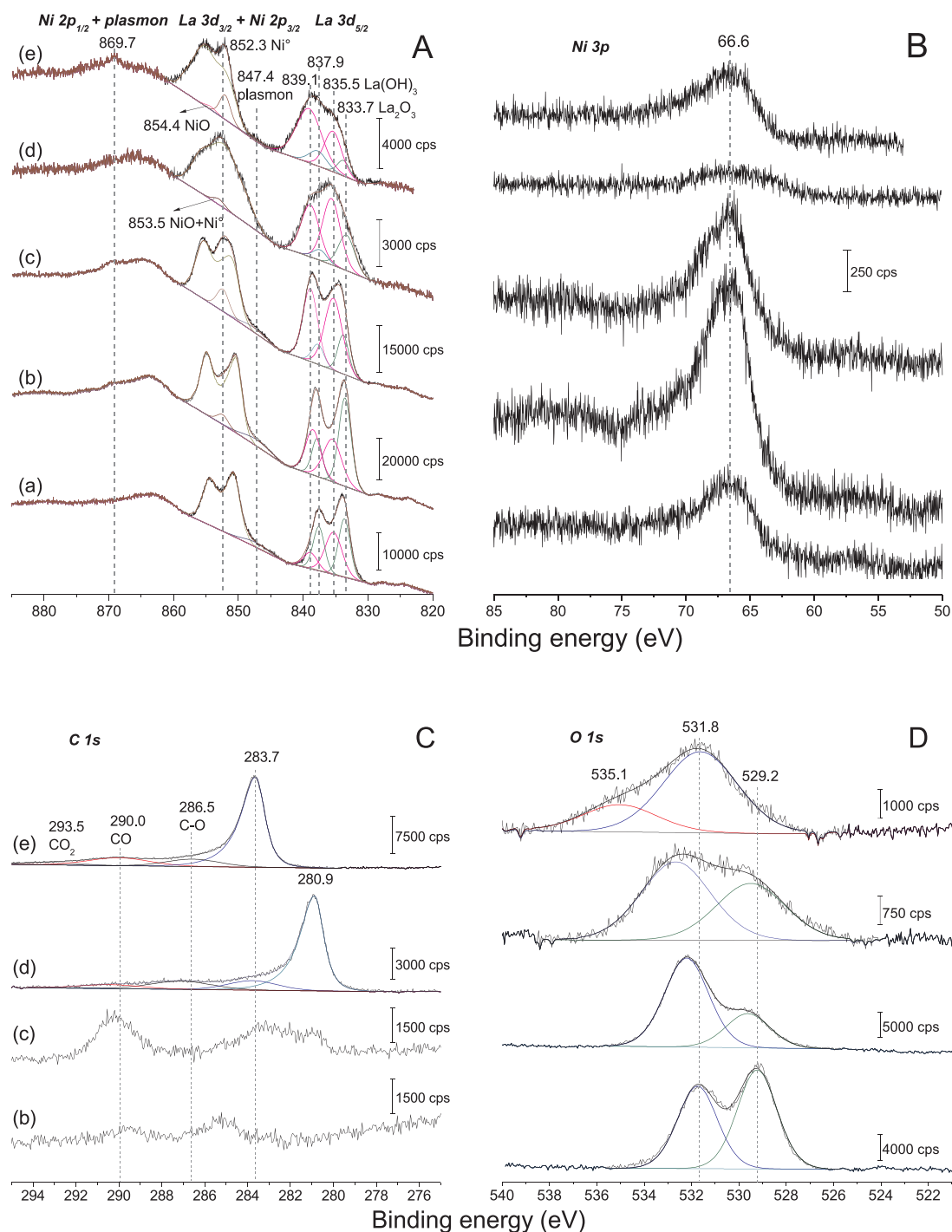


Fig. 7. XPS binding energies of LaNiO₃ catalyst under different treatments: (a) after reduction under H₂ at 1023 K and passivation; (b) sample “a” after reduction under H₂ at 773 K; (c) after DRM reaction at 823 K for 5 min; (d) after DRM reaction at 823 K for 30 min; (e) after DRM reaction at 823 K for 120 min. (A) La 3d and Ni 2p regions; (B) Ni 3p region; (C) C 1s region; (D) O 1s region.

preferentially oxidized, inhibiting the oxidation of the metallic phase. In our work, the oxidation of metallic Ni particles by CO₂ from the feed seems to occur over LaNiO₃ and LaNiO₃/Al₂O₃. This explains the increase in methane and CO₂ conversions in the first hours of the reaction since the NiO particles formed were reduced by the syngas produced during the reaction. Moreover, since the metallic Ni particles were oxidized at the beginning of the reaction, the CO formation decreased due to the occurrence of oxidation of CO to CO₂ over NiO particles. In the case of LaNiO₃/CeSiO₂ catalyst, ceria support is preferentially oxidized by CO₂ from the feed, preventing the formation of NiO. In order to investigate the oxidation state of nickel during reaction, *in situ* XPS

experiments were performed.

3.3. *In situ* XPS results

The analysis of the XPS results is rather complicated due to the overlapping of the La 3d_{3/2} and Ni 2p_{3/2} constituents, and also of the Ni 2p_{1/2} signal and a plasmon loss feature belonging to La 3d_{3/2}. Moreover, in many cases the intensity of Ni 2p is hardly discernible from other spectral characteristics.

The La 3d spectrum of LaNiO₃ shows the characteristic “double” structure (Fig. 7A). According to literature La 3d_{5/2} can be

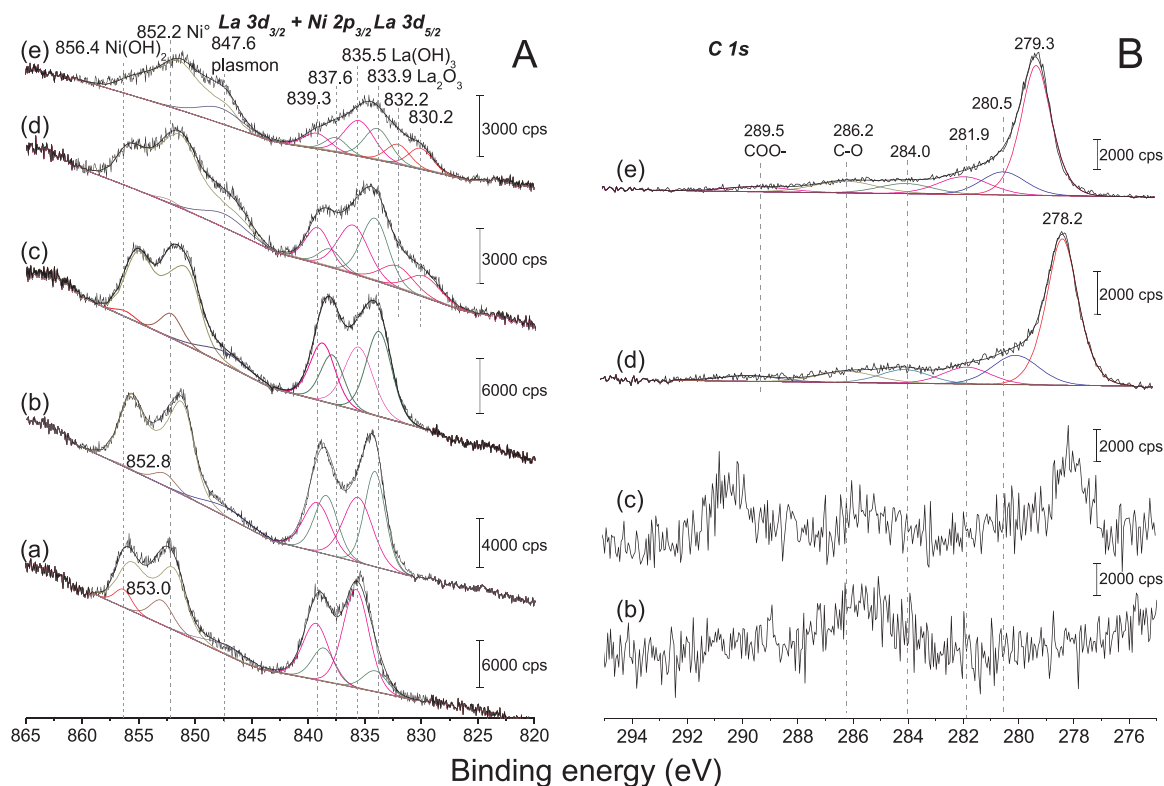


Fig. 8. XPS binding energies of LaNiO₃/Al₂O₃ catalyst. (a) after reduction under H₂ at 1023 K and passivation; (b) sample “a” after reduction under H₂ at 773 K; (c) after DRM reaction at 823 K for 5 min; (d) after DRM reaction at 823 K for 30 min; (e) after DRM reaction at 823 K for 120 min. (A) La 3d and Ni 2p regions; (B) C 1s region.

deconvoluted into four components. For the pre-reduced sample and after post-reduction the most intense component was found at 833.7 eV corresponding to the La 3d_{5/2} component in La₂O₃. The same component of the other less intense constituent is located at 835.5 eV and can be assigned to La(OH)₃ [35,36]. Peaks at 837.9 and 839.1 eV are the corresponding satellites of the La₂O₃ and La(OH)₃ components. Even after the 5th minute of the reaction with the CH₄ + CO₂ gas mixture, there is a noticeable change in the La 3d spectral shape. The intensity of the lower binding energy component attributed to La₂O₃ seems to decrease, while that of the other component enhances. However, La 3d spectra taken after the post-reduction show that the envelopes of the two distinct components are dissimilar. A new well resolved peak emerged at 852.3 eV and a little one within the broad plasmon loss feature 17.4 eV farther. These peaks were tentatively assigned to metallic nickel. After 30 min treatment, the Ni 2p 3/2 peak shifted to higher binding energies, which may indicate the appearance of another oxidation state beside the metallic Ni. After 120 min of reaction the Ni⁰ peak and a new component at 854.4 eV were identified. The latter one definitely cannot be assigned to metallic Ni.

In order to investigate the changes in the Ni oxidation state during reaction, the Ni 3p signal was also recorded (Fig. 7B). The 66.6 eV binding energy is characteristic of metallic nickel whereas the shoulder at higher BE corresponds to NiO [37,38]. The intensity of this peak attributed to metallic nickel changed throughout the experiment. The highest intensity was recorded in the reduced sample at 773 K. Then, the intensity of this peak continuously decreased during the reaction and almost disappeared after 30 min of TOS, which was accompanied by the appearance of a shoulder at higher BE. This result reveals that the surface of metallic Ni particles oxidized in the presence of the reaction mixture, in agreement with the catalytic tests. After 120 min TOS, the intensity of this peak increased, indicating that the NiO particles were reduced by the syngas produced during the reaction.

Unfortunately, no trends were observed in the changes of the C 1s and O 1s features. A characteristic asymmetric carbon peak was

detected at 280.9 eV after the 30th minute and at 283.7 eV after the 120th minute (Fig. 7C). These peaks can be assigned to different types of carbide or oxycarbide-like species [39–42].

The results on oxygen O 1s peak are somewhat more consequent (Fig. 7D). A single broad peak is observed in the pre-reduced sample. After post-reduction, this peak was split into two well resolved components located at 529.2 (lattice oxygen) and 531.8 eV, the former being the more intense. This feature could be due to oxygen from C=O and OH groups alike. During the reaction, the intensity of the higher binding energy component increased with respect to the other and shifted upward. In addition, a peak broadening also occurred, which indicates the presence of different oxygen compounds possessing very similar binding energies. After 120 min this peak shifted back to the position where it was after post-reduction and at the same time a new component emerged at 535.1 eV – possibly from water.

Apart from some interesting differences, the overall behavior of the supported samples was very similar. For LaNiO₃/Al₂O₃, no changes could be detected in the Al 2p signals. On the other hand, remarkable changes were observed on the La 3d spectra (Fig. 8A). After 30 min TOS, a clear new low binding energy shoulder was observed on both members of the La 3d doublet. Since their separation corresponds to that of La 3d, it might be supposed that these shoulders represent a sort of new lanthanum state. However, after 120 min the peak shapes of the La 3d doublets became dissimilar and it looks like the peaks lost intensity of La₂O₃ constituent. In this case the Ni 3p peak was hidden by the satellite of Al 2p and this prevents to follow the evolution of the Ni state during the reaction.

In the C 1s region there is a single intense peak between 281 and 282 eV and a shoulder around 285 eV in the pre-reduced sample (not shown). This latter one corresponds to the peak that is usually identified with adventitious carbon. The low binding energy major component might represent the existence of some carbide-like species probably created from adventitious carbon during the high temperature pretreatment. Another explanation could be that carbon supported on

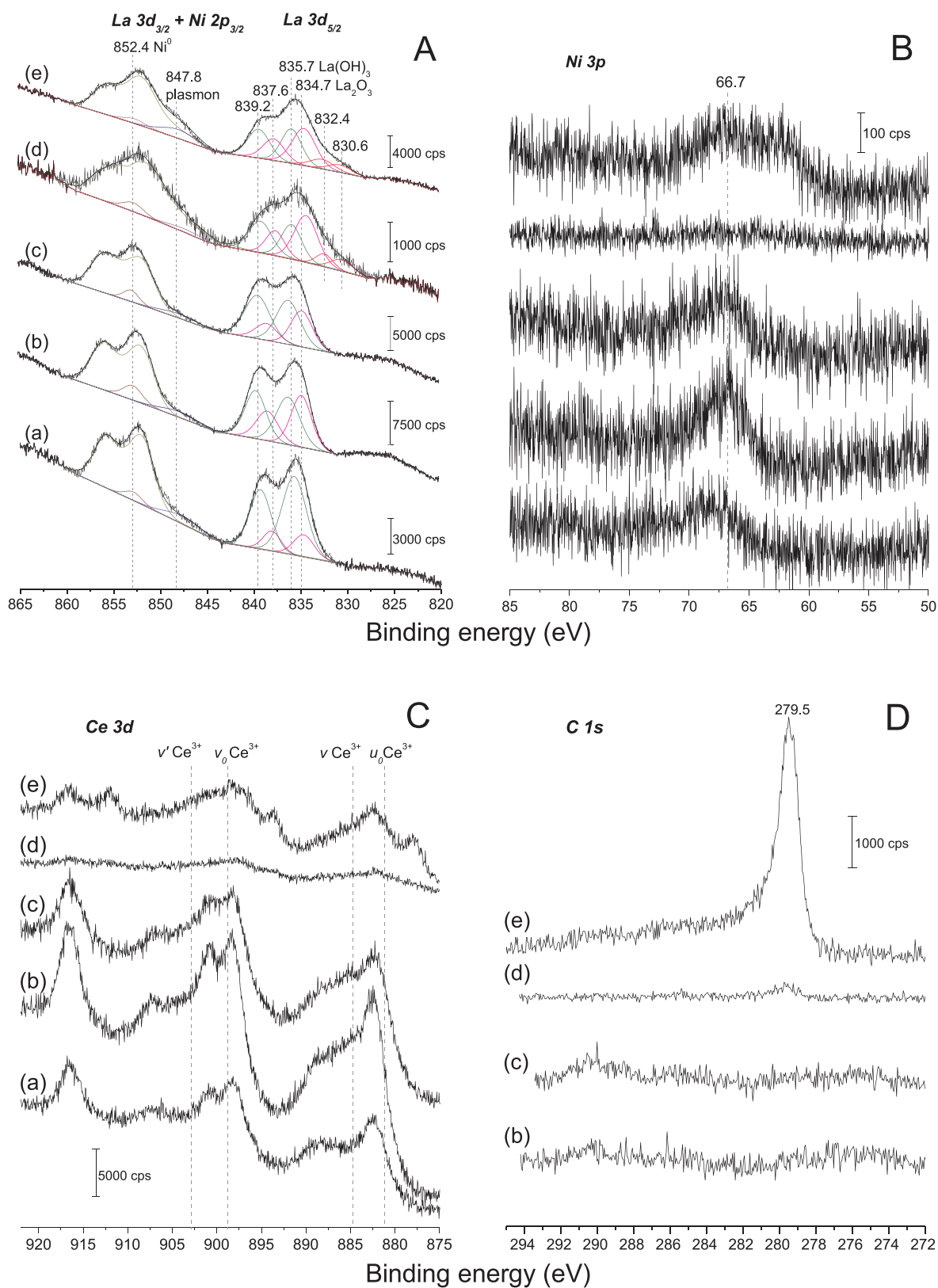


Fig. 9. XPS binding energies of LaNiO₃/CeSiO₂ catalyst. (a) after reduction under H₂ at 1023 K and passivation; (b) sample “a” after reduction under H₂ at 773 K; (c) after DRM reaction at 823 K for 5 min; (d) after DRM reaction at 823 K for 30 min; (e) after DRM reaction at 823 K for 120 min. (A) La 3d and Ni 2p regions; (B) Ni 3p region; (C) Ce 3d region; (D) C 1s region.

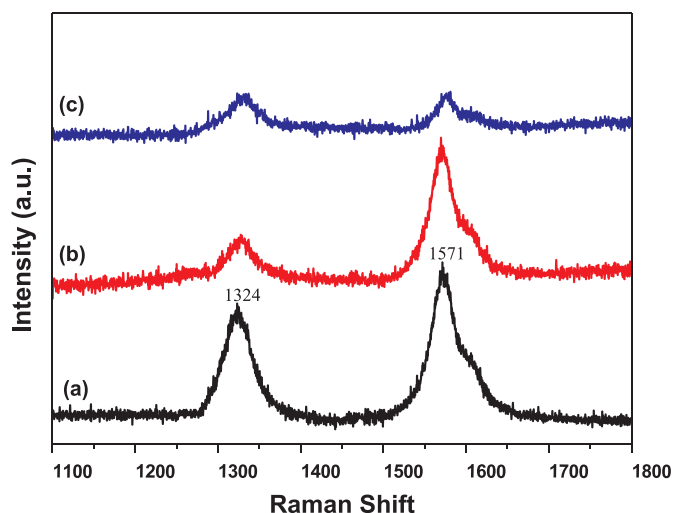


Fig. 10. Raman spectra of used catalysts after DRM at 1073 K: (a) LaNiO₃; (b) LaNiO₃/Al₂O₃; (c) LaNiO₃/CeSiO₂.

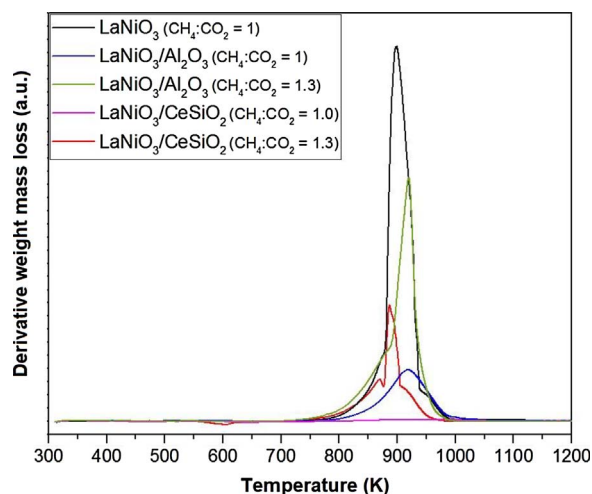


Fig. 11. TPO profiles of used catalysts after DRM at 1073 K.

La has as low binding energy as 281 eV. The post-reduction step eliminates this feature (Fig. 8B) but after the 30th minute a new peak could be detected at 278.2 eV with a long extending tail towards higher binding energies that likely also belongs to C 1s. After 120 min of reaction the C 1s intensity did not change, but the peak location shifted upwards by 1 eV. These C 1s components may be coupled to the low binding energy La 3d components and indicate the formation of carbides. However, the intensity of the peak at 284 eV assigned to carbide or oxycarbide-like species on the unsupported sample is very weak in this catalyst.

The O 1s feature consisted of two components (not shown), the

major one at 531.6 eV with constant peak area is characteristic of alumina. In the pre-reduced sample, a minor peak could also be resolved at 528.8 eV which was assigned to La-O bond. It vanished after post-reduction but a new, faint, but intensifying feature emerged at 527.0 eV in the reaction with the gas mixture due to some kind of metal-O bonding.

Spectra of LaNiO₃/SiCeO₂ are very much like those of alumina supported samples (Fig. 9). However, the component corresponding to La₂O₃ shifted about 1 eV higher that can be attributed to an interaction with the SiCeO₂ support. The new low binding energy lanthanum component formed after the 30th minute of the reaction was also observed. Although the intensities are much lower, the Ni 3p peak positions seem to be very similar to those of the unsupported samples. In addition, the intensity of this peak remains approximately constant after 5 and 120 min, indicating that the oxidation of metallic Ni is limited. However, there is a difference: after the 120th minute of the reaction the signal had a 'component' at lower binding energies which could not be explained. Its binding energy (~63.2 eV) is too low for Ni 3p.

A considerable reduction is seen on the Ce 3d spectra (Fig. 9C) even in the post-reduction stage compared to CeO₂. Based on the deconvolution of Ce 3d spectra the Ce(III)/[Ce(III) + Ce(IV)] ratio was calculated after different treatment. For the post-reduced sample, this ratio is 0.23 and increased to 0.31 after the 120th minute. Further reaction causes a massive intensity drop both in La 3d and Ce 3d and O 1s regions. This phenomenon cannot be explained by carbon deposition unlike in the case of the other two samples. Interestingly, after 120 min these peaks re-emerge from the background. The unusual structure of the Ce 3d signal at this stage can be the result of uneven charging of the sample owing to unidentified reasons. During the pre-reduction of the sample, the total amount of carbon could be removed. Only after the 120th min of the reaction was observed a C 1s component attributed to carbide carbon. In the O 1s region (not included), beside the initial OH (532.2 eV) and CeO₂ (530.1 eV) signals, unidentified new components emerged under the reaction at unusually low binding energies (527.4 and 525 eV).

3.4. Characterization of post-reaction catalysts after DRM at 1073 K

One of the main drawbacks of the DRM is catalyst deactivation mainly due to carbon deposition and metal sintering. In order to investigate the formation of carbon during the reaction, the post-reaction catalysts were characterized by Raman spectroscopy and TG. In situ XRD during DRM for 1 h was also carried out to determine the changes in Ni crystallite size.

The Raman spectra of the spent catalysts are presented in Fig. 10. The spectra show two bands in the range of 1200–1800 cm⁻¹, which are associated with the D and G vibration modes of carbon materials. The so-called D band is related to disordered-induced Raman scattering from sp² carbons [43]. The position and linewidth of this band allow distinguishing between the different allotropic forms of carbon. For instance, amorphous carbon exhibits a very broad linewidth

Table 4

Amount of carbon deposited on all catalysts after dry reforming of methane at 1073 K.

Catalyst	Reaction conditions	mgC/gcat/h	Reference
LaNiO ₃	T = 1073 K, CH ₄ :CO ₂ = 1:1	27.04	Our work
LaNiO ₃ /Al ₂ O ₃	T = 1073 K, CH ₄ :CO ₂ = 1:1	7.58	Our work
LaNiO ₃ /CeSiO ₂	T = 1073 K, CH ₄ :CO ₂ = 1:1	0.32	Our work
NiCu/Ce _{0.9} Gd _{0.1} O _{2-δ} (Commercial)	T = 1073 K, CH ₄ :CO ₂ = 1:1	12.2	[50]
NiCu/Ce _{0.9} Gd _{0.1} O _{2-δ} (Co-precip.)	T = 1073 K, CH ₄ :CO ₂ = 1:1	7.7	[50]
NiCu/Ce _{0.9} Gd _{0.1} O _{2-δ} (Impreg.)	T = 1073 K, CH ₄ :CO ₂ = 1:1	2.4	[50]
La _{0.8} Sr _{0.2} Ni _{0.8} Cu _{0.2} O ₃	T = 1073 K, CH ₄ :CO ₂ :N ₂ = 1:1:1	225	[51]
La _{0.8} Sr _{0.2} Ni _{0.8} Cr _{0.2} O ₃	T = 1073 K, CH ₄ :CO ₂ :N ₂ = 1:1:1	250	[51]
La _{0.8} Sr _{0.2} Ni _{0.8} Co _{0.2} O ₃	T = 1073 K, CH ₄ :CO ₂ :N ₂ = 1:1:1	50	[51]

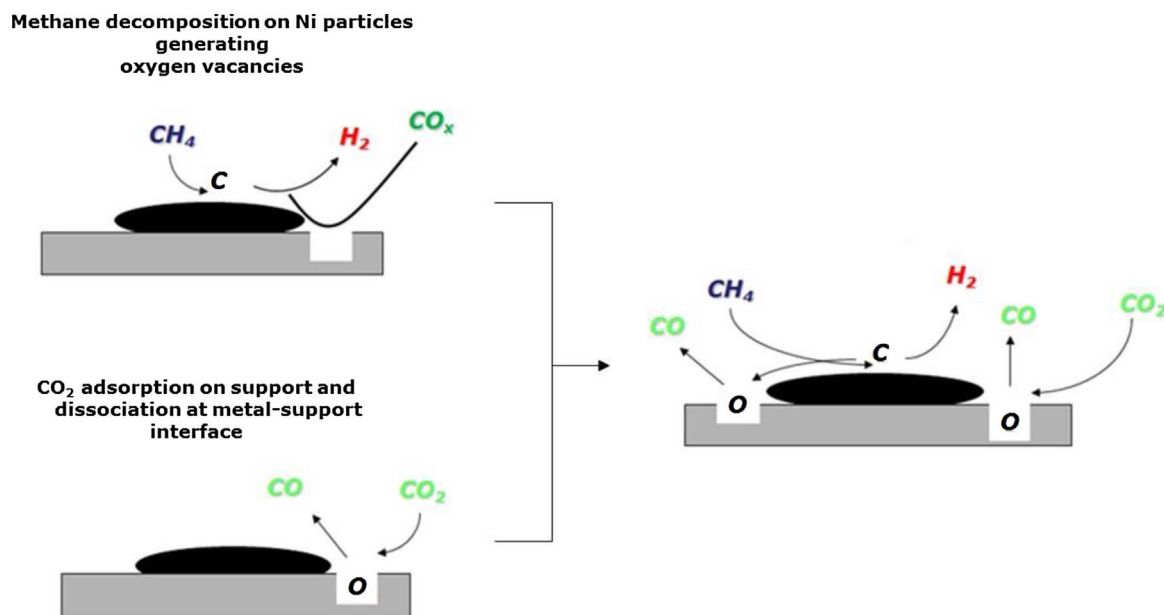


Fig. 12. Scheme for the dual path mechanism for DRM over Ni supported on CeSiO₂.

($> 100 \text{ cm}^{-1}$). The D band in the range of $1285\text{--}1300 \text{ cm}^{-1}$ with a linewidth of $10\text{--}30 \text{ cm}^{-1}$ is characteristic of single-walled carbon nanotube (SWNT). Crystalline graphite-like forms and multi-walled carbon nanotubes (MWNT) show a D band at around $1305\text{--}1330 \text{ cm}^{-1}$ and a width of about $30\text{--}60 \text{ cm}^{-1}$. The band G corresponds to the in-plane bond-stretching motion of pairs of C sp^2 atoms [44]. For carbon nanotubes, this band splits into two peaks associated with the atomic displacements along circumferential (G-) and axial direction (G +) of the tube [45].

In this work, the D band at 1324 cm^{-1} with a linewidth varying from 34 to 58 cm^{-1} and a G band at 1571 and 1600 cm^{-1} suggests the presence of MWNT. In addition, the intensities of these bands decreased in the following order: $\text{LaNiO}_3 > \text{LaNiO}_3/\text{Al}_2\text{O}_3 \gg \text{LaNiO}_3/\text{CeSiO}_2$. The Raman spectra of $\text{LaNiO}_3/\text{CeSiO}_2$ indicate that carbon deposition is very low over this catalyst.

Fig. 11 shows the first derivative of the weight loss curve as a function of temperature that can be associated with the TPO profiles of LaNiO_3 and supported LaNiO_3 catalysts after DRM at 1073 K under different CH_4/CO_2 molar ratios. After reaction under $\text{CH}_4/\text{CO}_2 = 1.0$, LaNiO_3 and $\text{LaNiO}_3/\text{Al}_2\text{O}_3$ catalysts exhibited one peak at 898 and 916 K , respectively. However, no peaks were observed on the TPO profile of $\text{LaNiO}_3/\text{CeSiO}_2$ catalyst. The TPO profiles of $\text{LaNiO}_3/\text{Al}_2\text{O}_3$ and $\text{LaNiO}_3/\text{CeSiO}_2$ catalysts after reaction under $\text{CH}_4/\text{CO}_2 = 1.3$ reveals peaks at 880 and 920 K . According to the literature [46–49], the oxidation peak located below 673 K is ascribed to amorphous carbon whereas the peak above 773 K corresponds to carbon nanotubes (SWNT and MWNT). The oxidation of graphite occurs at higher temperatures ($\sim 973 \text{ K}$). Therefore, our TPO profile indicates the presence of filamentous carbon (SWNT and/or MWNT), which agrees with the Raman spectra.

The amount of carbon deposited on all catalysts after DRM at 1073 K , as determined by TG analysis, is listed in Table 4. The largest amount of carbon was formed on LaNiO_3 . Supporting LaNiO_3 significantly decreased the amount of deposited carbon. For alumina, the amount of carbon was approximately $1/3$ of that one for the unsupported LaNiO_3 . The deposition of LaNiO_3 over CeSiO_2 practically eliminates the formation of carbon. Table 4 also reports some carbon formation rate from the literature for comparison [50,51]. The amount of carbon deposited over $\text{LaNiO}_3/\text{CeSiO}_2$ is very low in comparison to values presented in the literature.

The mechanism of coke formation over supported Ni catalysts

during steam or CO_2 reforming of methane is well described in the literature [12,52–55]. According to the dual path mechanism for DRM [19–21], the first step involves the dissociation of methane on nickel surface, producing hydrogen and highly reactive carbon species (C_α) [54]. The second path is the reaction of this carbon with oxygen from the support, keeping the surface of the catalyst free of carbonaceous residues. This oxygen is formed during the dissociative adsorption of CO_2 and reoxidation of the support. However, if the rate of methane dissociation is faster than the rate of carbon oxidation, C_α formed may undergo polymerization to less active carbon (C_β). As a result, it may accumulate on the surface or may dissolve into the nickel lattice. It is suggested that nickel carbide is an essential intermediate of this process [54,55]. The dissolution of carbon into the Ni crystallite is the first step for the nucleation and growth of carbon filaments (e.g., whiskers). Then, the balance between the rate of methane decomposition and the rate of cleaning determines the stability of the catalyst. Therefore, in this dual path mechanism, the role of the support is very important. It participates in the dissociative adsorption of CO_2 near the metal particles, transferring oxygen to the coked metal and greatly accelerating the removal of carbon from the metal [22,56]. This is the case of ceria and ceria-mixed oxides that exhibit a very high oxygen exchange capacity due to their ability to reversibly change oxidation states between Ce^{4+} and Ce^{3+} . The *in situ* XPS experiments showed the presence of a high fraction of Ce^{3+} during the reaction, demonstrating that the redox cycle is operational for DRM over $\text{LaNiO}_3/\text{CeSiO}_2$ catalyst. Fig. 12 shows a scheme for this dual path mechanism.

In our work, the lower carbon formation over $\text{LaNiO}_3/\text{CeSiO}_2$ catalysts could be attributed to the higher oxygen storage capacity of ceria support. The higher oxygen mobility of ceria favors the mechanism of carbon removal, improving catalyst stability. This was evidenced by the *in situ* XPS experiments that did not detect the formation of nickel carbide species. In fact, the formation of carbide was inhibited due to the oxidation of carbon by the oxygen of ceria support as soon as it is formed, eliminating carbon deposition.

In addition, *in situ* XRD revealed that the metal-Ce interaction also inhibited metal sintering during the reaction. The growth in the Ni crystallite size during the DRM was lower for the $\text{LaNiO}_3/\text{CeSiO}_2$ catalyst (Table 2), which also contributes for the lower carbon formation. This result also demonstrated that the increase in the methane and CO_2 conversion is likely due to reduction of the metal particles that were oxidized by the feed since the increase in the Ni crystallite size should

decrease the conversion.

4. Conclusions

Supporting LaNiO_3 over CeSiO_2 significantly decreased the deposition of carbon during the DRM. The *in situ* XPS experiments revealed that the fraction of Ce^{3+} modified during the reaction. The reversible change of ceria oxidation states between Ce^{4+} and Ce^{3+} indicates that CeSiO_2 support exhibits a high oxygen storage/release capacity. This high oxygen mobility of CeSiO_2 promotes the removal of carbon as soon as it is formed, inhibiting the formation of nickel carbide, the first step for the nucleation and growth of carbon filaments. The metal-Ce interaction also inhibited metal sintering and promoted catalyst stability.

Acknowledgements

The authors thank CNPq (Conselho Nacional de Desenvolvimento Científico e Tecnológico) and CAPES (Coordenação de Aperfeiçoamento de Pessoal de Ensino Superior) for supporting this research and the scholarship received.

References

- [1] J.H. Edwards, A.M. Maitra, Fuel Process. Technol. 42 (1995) 269–289.
- [2] A. Erdohelyi, J. Cserenyi, F. Solymosi, J. Catal. 141 (1993) 287–299.
- [3] M.C.J. Bradford, M.A. Vannice, Catal. Rev. Sci. Eng. 41 (1999) 1–42.
- [4] M.S. Fan, A.Z. Abdullah, S. Bathia, ChemCatChem 1 (2009) 192–208.
- [5] P.M. Mortensen, I. Dybkjaer, Appl. Catal. A: Gen. 495 (2015) 141–151.
- [6] K. Seshan, H.W. ten Barge, A.N.J. van Keulen, J.R.H. Ross, Stud. Surf. Sci. Catal. 81 (1994) 285–290.
- [7] J.A. Lercher, J.H. Bitter, W. Halley, W. Niessen, K. Seshan, Stud. Surf. Sci. Catal. 101 (1996) 463–472.
- [8] J.R. Rostrup Nielsen, J.H. Bak Hansen, J. Catal. 144 (1993) 38–49.
- [9] V.A. Tsipouriari, X.E. Verykios, Catal. Today 64 (2001) 83–90.
- [10] M.C.J. Bradford, M.A. Vannice, Appl. Catal. A 142 (1996) 97–122.
- [11] A. Kambolis, H. Matralis, A. Trovarelli, C. Papadopolou, Appl. Catal. A 377 (2010) 16–26.
- [12] J.R. Rostrup-Nielsen, J. Sehested, J. Norskov, Adv. Catal. 47 (2002) 65–139.
- [13] M.A. Pena, J.L.G. Fierro, Chem. Rev. 101 (2001) 1981–2018.
- [14] S.M. Lima, J.M. Assaf, M.A. Pena, J.L.G. Fierro, Appl. Catal. A 311 (2006) 94–104.
- [15] S.M. de Lima, M.A. Pena, J.L.G. Fierro, J.M. Assaf, Catal. Lett. 124 (2008) 195–203.
- [16] G. Valderrama, A. Kiennemann, M.R. Goldwasser, J. Power Sources 195 (2010) 1765–1771.
- [17] I. Rivas, J. Alvarez, E. Pietri, M.J. Perez-Zurita, M.R. Goldwasser, Catal. Today 149 (2010) 388–393.
- [18] N. Wang, X. Yu, Y. Wang, W. Chu, M. Liu, Catal. Today 212 (2013) 98–107.
- [19] J.R.H. Ross, A.N.J. van Keulen, M.E.S. Hegarty, K. Seshan, Catal. Today 30 (1996) 193–199.
- [20] A.M. O'Connor, F.C. Meunier, J.R.H. Ross, Stud. Surf. Sci. Catal. 119 (1998) 819–824.
- [21] S.M. Stagg-Williams, F. Noronha, G. Fendley, D.E. Resasco, J. Catal. 194 (2000) 240–249.
- [22] F.B. Noronha, E.C. Fendley, R.R. Soares, W.E. Alvarez, D.E. Resasco, Chem. Eng. J. 82 (2001) 21–31.
- [23] A.A.A. Da Silva, N. Bion, F. Epron, S. Baraka, F.C. Fonseca, R.C. Rabelo-Neto, L.V. Mattos, F.B. Noronha, Appl. Catal. B 206 (2017) 626–641.
- [24] A. Trovarelli, M. Boaro, E. Rocchini, C. de Leitenburg, G. Dolcetti, J. Alloys Compd. 323–324 (2001) 584.
- [25] A.A.A. da Silva, L.O.O. da Costa, L.V. Mattos, F.B. Noronha, Catal. Today 213 (2013) 25–32.
- [26] J. Wei, E. Iglesia, J. Catal. 224 (2004) 370–383.
- [27] L. Coronel, J.F. Munera, E.A. Lombardo, L.M. Cornaglia, Appl. Catal. A 400 (2011) 185–194.
- [28] E. Ruckenstein, Y.H. Hu, Appl. Catal. A 154 (1997) 185–205.
- [29] F.B. Passos, E.R. de Oliveira, L.V. Mattos, F.B. Noronha, Catal. Today 101 (2005) 23–30.
- [30] E. Rocchini, A. Trovarelli, J. Llorca, G.W. Graham, W.H. Weber, M. Maciejewski, A. Baiker, J. Catal. 194 (2000) 461–478.
- [31] J. Hu, C. Yu, Y. Bi, L. Wei, J. Chen, X. Chen, Chin. J. Catal. 35 (2014) 8–20.
- [32] V.V. Kharton, A.P. Viskup, E.N. Naumovich, F.M.B. Marques, J. Mater. Chem. 9 (1999) 2623–2629.
- [33] E.C. Faria, R.C.R. Neto, R.C. Colman, F.B. Noronha, Catal. Today 228 (2014) 138–144.
- [34] K. Takanabe, K. Nagaoka, K. Nariai, K. Aika, J. Catal. 230 (2005) 75–85.
- [35] S. Mickevicius, S. Grebinkij, V. Bondarenka, B. Vengalis, K. Sliuziene, B.A. Orlowski, W. Osinniy, W. Drube, J. Alloys Compd. 423 (2006) 107–111.
- [36] Y.A. Teterin, A.M. Lebedev, K.E. Ivanov, J. Electron. Spectrosc. Relat. Phenom. 137 (2004) 607–612.
- [37] F. El Gabaly, K.F. McCarty, H. Bluhm, A.H. McDaniel, Phys. Chem. Chem. Phys. 15 (2013) 8334–8341.
- [38] H. Lei, Z. Song, X. Bao, X. Mu, B. Zong, E. Min, Surf. Interface Anal. 32 (2001) 210–213.
- [39] S. Sinharoy, L.L. Levenson, Thin Solid Films 53 (1978) 31–36.
- [40] P. Delporte, F. Meunier, C. Pham-Huu, P. Vennequies, M.J. Ledoux, J. Guille, Catal. Today 23 (1995) 251–267.
- [41] N.K. Huang, D.Z. Wang, Q. Xiong, B. Yang, Nucl. Instrum. Methods Phys. Res. B 207 (2003) 395–401.
- [42] L. Guzzi, G. Stefler, O. Gestzi, I. Sajo, Z. Paszti, A. Tompos, Z. Schay, Appl. Catal. A 375 (2010) 236–246.
- [43] T. Belin, F. Epron, Mater. Sci. Eng. B 119 (2005) 105–118.
- [44] A.C. Ferrari, J. Robertson, Phys. Rev. B 61 (2000) 14095–14107.
- [45] M.S. Dresselhaus, G. Dresselhaus, M. Hofmann, Vib. Spectrosc. 45 (2007) 71–81.
- [46] S.M. de Lima, A.M. da Silva, L.O.O. da Costa, J.M. Assaf, G. Jacobs, B.H. Davis, L.V. Mattos, F.B. Noronha, Appl. Catal. A 377 (2010) 181–190.
- [47] A.E. Galetti, M.F. Gomez, L.A. Arrua, M.C. Abello, Appl. Catal. A 348 (2008) 94–102.
- [48] M.C. Sanchez-Sanchez, R.M. Navarro, J.L.G. Fierro, Int. J. Hydrogen Energy 32 (2007) 1462–1471.
- [49] B. Kitiyanan, W.E. Alvarez, J.H. Harwell, D.E. Resasco, Chem. Phys. Lett. 317 (2000) 497–503.
- [50] G. Bonura, C. Cannilla, F. Frusteri, Appl. Catal. B 121 (2012) 135–147.
- [51] K. Sutthiumporn, T. Maneerung, Y. Kathiraser, S. Kawi, Int. J. Hydrogen Energy 37 (2012) 11195–11207.
- [52] J.R. Rostrup-Nielsen, Catal. Today 18 (1993) 305–324.
- [53] J.R. Rostrup-Nielsen, T. Rostrup-Nielsen, CATTECH 6 (2002) 150–159.
- [54] D.L. Trimm, Catal. Today 37 (1997) 233–238.
- [55] D.L. Trimm, Catal. Today 49 (1999) 3–10.
- [56] J.H. Bitter, W. Hally, K. Seshan, J.G. van Ommen, J.A. Lercher, Catal. Today 29 (1996) 349–353.